INORGANIC CHEMISTRY
FRONTIERS

CHINESE CHEMICAL SOCIETY

ROYAL SOCIETY OF CHEMISTRY

RESEARCH ARTICLE

View Article Online
View Journal

Cite this: DOI: 10.1039/d6qi00520a

Few layer phosphorene/reduced graphene oxide/graphitic carbon nitride ternary heterojunctions for sustainable photoredox C–H functionalization of heteroarenes

Zafer Eroglu, †[a,d] Ozge Turbedaroglu, †[b] Temirlan Kubanaliev,[a] Sila Alemdar,[a] Haydar Kilic *[b] and Onder Metin *[a,c]

Received 18th March 2026,
Accepted 18th May 2026

DOI: 10.1039/d6qi00520a

rsc.li/frontiers-inorganic

Building upon our research on the rational design of metal-free heterojunctions as multifunctional photocatalysts, we report herein a novel ternary heterojunction comprising few-layer phosphorene (FLP), reduced graphene oxide (rGO), and graphitic carbon nitride (g-CN) (FLP/rGO/g-CN) for the visible-light-driven C–H arylation of heteroarenes. Comprehensive characterization techniques confirmed the successful integration of FLP, rGO, and g-CN into a well-defined heterostructure with intimate interfacial contact. Optimization studies on the photoredox C–H arylation of heteroarenes revealed that 30 wt% FLP within rGO/g-CN exhibited superior performance, outperforming individual constituents and the binary heterojunction (rGO/g-CN). Under the optimized reaction conditions, the FLP/rGO/g-CN heterojunction efficiently mediated the arylation of furan derivatives with aryl diazonium salts, achieving yields of up to 94%, while thiophene derivatives furnished moderate yields (up to 84%) with electron-deficient aryl groups. Solid-state NMR (ssNMR) analysis reveals strong interactions between the central nitrogen atoms of the tri-s-triazine units and the FLP species as well as rGO, leading to an increased local electron density that synergistically enhances photocatalytic activity compared to the pristine materials. Mechanistic studies, including radical scavenger experiments and charge transfer analysis, revealed a synergistic nonclassical type-I heterojunction mechanism that promotes efficient spatial separation and directional migration of photogenerated charge carriers, thereby minimizing their recombination. Furthermore, the FLP/rGO/g-CN heterojunction demonstrated excellent recyclability, maintaining its high activity over five consecutive cycles without significant loss, underscoring its robustness and high chemical stability. This study highlights the potential of rationally engineered 2D-based ternary heterostructures as sustainable and high-performance photocatalysts for solar-driven C–H functionalization, offering insights into the design of advanced metal-free catalytic systems for organic transformations.

Introduction

Synthetic methods for C–H functionalization represent a continually evolving area of research, aimed at achieving highly selective, mild, atom-efficient, and cost-effective strategies for the construction and late-stage modification of high-value organic molecules.[1,2] Among these strategies, photocatalysis has emerged as a sustainable paradigm, leveraging solar energy to enable low-energy and environmentally benign chemical transformations.[3,4] As a pollution-free and renewable energy source, sunlight offers significant advantages by minimizing the ecological impact while maintaining the cost efficiency.[5,6] However, a major limitation arises from the fact that most organic substrates lack intrinsic redox-active functional groups, hindering efficient photocatalytically driven bond cleavage and formation.[7] Additionally, certain reactions with high activation energies, particularly C–H activation and subsequent functionalization processes, are often difficult to initiate using light as the sole energy source.[2,8] To overcome such high activation energy, various metal complexes have been introduced for a wide range of applications as photocatalysts due to their versatile redox properties and broad

---

[a] Department of Chemistry, College of Sciences, Koç University, 34450 Sarıyer, İstanbul, Türkiye. E-mail: ometin@ku.edu.tr
[b] Department of Chemistry, Faculty of Sciences, Atatürk University, 25240 Erzurum, Türkiye. E-mail: hydk@atauni.edu.tr
[c] Koç University Surface Science and Technology Center (KUYTAM), 34450 Sarıyer, İstanbul, Türkiye
[d] Kocaeli University, Faculty of Arts and Sciences, Department of Chemistry, 41001 Kocaeli, Türkiye

† The authors contributed equally to this work.

applicability.[9–12] However, their use is hampered by several drawbacks, including high cost, scarcity, toxicity, and environmental persistence, alongside issues such as thermal instability and catalyst deactivation. In response, many researchers have contributed to this field by developing metal-free photocatalysts[13–17] yet a critical unresolved challenge lies in their efficient separation and recyclability from reaction mixtures. This has driven growing interest in designing robust, economical, and reusable catalytic systems. Within this framework, metal-free semiconductor-based photocatalysts have emerged as a promising alternative due to their favorable sustainability and operational advantages.[18,19]

Among emerging candidates, the use of two-dimensional (2D) semiconductor materials consisting of abundant elements as photoredox catalysts in organic transformations is a promising path for researchers.[20–23] Notably, the pnictogen family (*e.g.*, 2D black phosphorus (BP or phospherene (FLP)) and bismuthene) has attracted considerable attention due to their tunable bandgaps, broad visible-to-NIR light absorption, layered structures, and high charge-carrier mobility.[24–27] Building on our previous work, we have demonstrated that heterogeneous photocatalytic systems based on few-layer phoshorene (FLP) and bismuthene offer significant advantages over conventional homogeneous catalysts for photoredox C–H arylation reactions.[28,29] However, the broader application of FLP remains limited by its low chemical stability, as it is sensitive to moisture and oxygen, leading to degradation. To address this challenge, we previously engineered BP-based heterojunctions by coupling FLP with functionalized 2D materials such as graphitic carbon nitride (g-CN) and reduced grapheneoxide (rGO) to form binary heterojunctions.[30,31] rGO offers a large surface area, excellent electrical conductivity and exceptional thermal stability, making it an efficient electron reservoir.[32–34] On the other hand, g-CN is widely recognized for its abundance, low cost, chemical robustness, and suitable bandgap (~2.7 eV), positioning it as a benchmark material in metal-free photocatalysis.[35] By strategically integrating BP into a binary rGO/g-CN heterostructure, we hypothesized that the resulting ternary heterojunction would combine the unique benefits of all three components, namely enhancing charge separation, boosting the photocatalytic performance, and, crucially, improving FLP's stability under ambient conditions.

In this perspective, we introduce herein a FLP/rGO/g-CN ternary heterojunction as a reusable, metal-free photocatalyst for efficient C–H arylation reactions under visible-light irradiation. Comprehensive characterization of the FLP/rGO/g-CN heterojunctions *via* advanced instrumental techniques revealed strong interfacial coupling between the constituent phases, facilitating efficient photogenerated charge separation and transfer, which collectively contribute to the significantly enhanced photocatalytic activity. To identify the optimal photocatalyst composition, where the components synergistically form a heterojunction with the best photocatalytic activity for the photoredox C–H arylation of heteroarenes, binary and ternary heterojunctions were systematically prepared with varying component ratios in a stepwise manner. Among them, the use of an FLP/rGO/g-CN ternary heterojunction composed of 30 wt% FLP demonstrated superior activity in the C–H arylation compared to its pristine materials. The scope and limitations of the designed ternary heterojunction were explored using seven different heteroarenes and twelve different aryl diazonium salts, yielding a total of 30 distinct biaryl products. To elucidate the role of the FLP/rGO/g-CN heterojunction in the C–H arylation mechanism, a series of radical scavenger experiments and charge transfer analyses were conducted. The results confirmed that the nonclassical type-I heterojunction mechanism is responsible for the enhanced photocatalytic performance, which is attributed to improved photophysical properties and more efficient charge separation. Furthermore, the heterogeneous nature and reusability of the FLP/rGO/g-CN heterojunction were confirmed through a model reaction, showing no significant loss in catalytic activity even after five consecutive cycles.

Experimental section

Synthesis of BP crystals

BP crystals were synthesized using a modified low-pressure chemical vapor transport (CVD) method.[36] The detailed synthesis procedure is provided in the SI.

Synthesis of reduced graphene oxide (rGO)

rGO was synthesized through a two-step process: initially, graphene oxide (GO) was prepared using a modified Hummers' method,[37] followed by its reduction using *N*,*N*-dimethylformamide (DMF) as the reducing agent. The detailed synthesis procedure is provided in the SI.

Synthesis of g-CN

g-CN was synthesized *via* thermal polycondensation of urea.[38] The detailed synthesis procedure is provided in the SI.

Synthesis of the FLP/rGO/g-CN heterojunction photocatalyst

A two-stage optimization strategy was employed to prepare the ternary FLP/rGO/g-CN heterojunction photocatalyst for enhanced activity in photoredox C–H activation reactions.[30,31] Initially, the binary rGO/g-CN system was synthesized at varying ratios, and the composition yielding the highest photocatalytic activity was identified. This optimized ratio was then maintained while FLP was incorporated at different concentrations to determine the optimal ternary composition.

For this purpose, predetermined amounts of rGO and g-CN were individually dispersed in ethanol and sonicated for 1 hour. The rGO dispersion was then added dropwise to the g-CN suspension, followed by 4 additional hours of sonication to ensure homogeneous dispersion and strong interfacial interactions. The resulting mixture was centrifuged at 7500 rpm for 12 minutes, and the solid product was dried under vacuum.

For the FLP/rGO/g-CN heterojunction, bulk BP was dispersed in DMF and subjected to 12 hours of sonication to achieve exfoliation. The resulting dispersion was centrifuged at 2000 rpm for 10 minutes to remove unexfoliated BP, yielding a stable FLP/DMF colloidal suspension. Separately, the optimized rGO/g-CN mixture was dispersed in DMF and sonicated for 1 hour, and then added dropwise to the FLP dispersion while maintaining sonication. The reaction mixture was further sonicated for 5 hours to promote strong interactions between the 2D nanostructures. The final material was isolated by centrifugation at 12 000 rpm for 10 minutes, washed multiple times with ethanol to remove DMF, and dried under vacuum at 50 °C.

Synthesis of aryl diazonium tetrafluoroborates

According to a reported procedure,[39] to a solution of corresponding aniline (10 mmol, 1 equiv.) in ethanol (2 mL) and water (2 mL) was added aqueous tetrafluoroboric acid (48 wt%, 2.0 equiv.). After stirring for 20 min at room temperature, the reaction mixture was cooled down to 0 °C using an ice-water bath and a solution of *tert*-butyl nitrite (20 mmol, 2.0 equiv.) was added dropwise under 0 °C. After the addition was completed, the mixture was stirred for 1 hour at room temperature. Then, diethylether (25 mL) was added to the reaction solution; the resulting precipitate was collected by filtration and washed with cold diethyl ether (3 × 10 mL) and dried under vacuum. The crude product was used in next step without further purification.

General procedure for the photoredox C–H arylation reaction

The photocatalyst in 1 mL of dry DMSO was placed in a jacketed flask. The corresponding aryl diazonium salt (0.25 mmol) and heteroarene (10 mmol) were added. Then, the jacketed flask was sealed with a septum, placed in the photoreactor system under white light (150 W, 13 330 lumens, UV cutoff, 140 mW cm^{-2}), and stirred with a magnetic stir bar at room temperature for 90 min. Finally, the mixture was diluted by the addition of ethyl acetate (10 mL) and washed with brine (3 × 10 mL). The combined organic phases were dried over Na_2SO_4 and the solvent was removed under vacuum. The residue was purified by thin layer chromatography on silica gel using EtOAc/hexane.

Results and discussion

Photocatalyst characteristics

The integration of g-CN with rGO is expected to enhance the photochemical stability, electronic structure, and diverse chemical properties of g-CN owing to the superior electrical conductivity of rGO, which facilitates efficient electron mobility. The further incorporation of FLP into the rGO/g-CN binary heterostructure not only extends the optical absorption range from visible to near-infrared (NIR), but also helps mitigate the inherent stability challenges associated with FLP.[37] The ternary FLP/rGO/g-CN heterojunction is rationally designed for superior performance in photoredox C–H functionalization reactions due to improved charge separation and light absorption. To gain a synergistic effect among the materials, in which the binary and ternary heterojunctions exhibit superior photocatalytic performance, a systematic two-stage optimization process was conducted to determine the optimal composition of the FLP/rGO/g-CN heterojunction photocatalyst, as detailed in the Experimental section. In the first stage, the rGO content in the rGO/g-CN binary system was varied, revealing that the highest photocatalytic activity was achieved by using 1 wt% rGO while higher rGO loadings yielded lower product formation reducing the effective photon utilization by the photocatalyst.[18] rGO can lead to significant absorption of incident light by itself despite enhancing charge transport. This finding underscores the importance of balancing the conductivity and light absorption to maximize the photocatalytic efficiency. In the second stage, the FLP content in the ternary system was optimized, with the highest activity observed at 30 wt% FLP, indicating its crucial role in further enhancing charge separation and light harvesting. Following optimization of the constituents in the ternary heterojunction, the most efficient FLP/rGO/g-CN heterojunction based on its photocatalytic activity in the model reaction was subjected to comprehensive structural and spectroscopic characterization to elucidate photocatalytic activity.

To investigate the crystalline properties of the synthesized materials, X-ray diffraction (XRD) analysis was performed, and the diffraction patterns of g-CN, rGO/g-CN, and FLP/rGO/g-CN photocatalysts are presented in Fig. 1a. The diffraction peak at $2\theta = 12.7°$ can be indexed to the in-plane structural ordering of the g-CN (100) reflection, while the one observed at $2\theta = 27.1°$ was attributed to the interlayer stacking of conjugated aromatic systems.[40] Additionally, diffraction peaks characteristic of orthorhombic FLP are detected at $2\theta = 16.7°$, 33.6°, 34.5°, and 52.5°, corresponding to the (020), (040), (111), and (060) crystal planes of BP, respectively (PDF no. 40-444).[41] A shift toward smaller 2θ values in these diffraction peaks compared to standard reference values suggests an increased interlayer spacing, likely due to the interactions among FLP, rGO, and g-CN. The absence of distinct rGO peaks in the XRD pattern is attributed to its lower loading amount (1 wt% rGO) relative to other components and its predominantly amorphous nature. To investigate the interactions involving the polar functional groups in g-CN-based binary and ternary heterojunctions, Fourier-transform infrared (FTIR) spectroscopy was performed as shown in Fig. 1b. The broad absorption band centered at 3235.9 cm^{-1}, similar to that of g-CN, corresponds to the stretching vibrations of N–H while O–H functional groups of rGO overlapped in the same region.[36] The characteristic peak at 807 cm^{-1} is attributed to the out-of-plane bending vibrations of heptazine units, confirming the retention of the structural framework of g-CN.[38] Additionally, the absorption bands observed in the range of 1200–1600 cm^{-1} correspond to the C–N stretching vibrations within the conjugated heptazine rings of g-CN, indicating the presence of strong interactions within the heterojunction structure. To further support the structural characterization obtained from XRD and FTIR, Raman spectroscopy was performed, and the corresponding

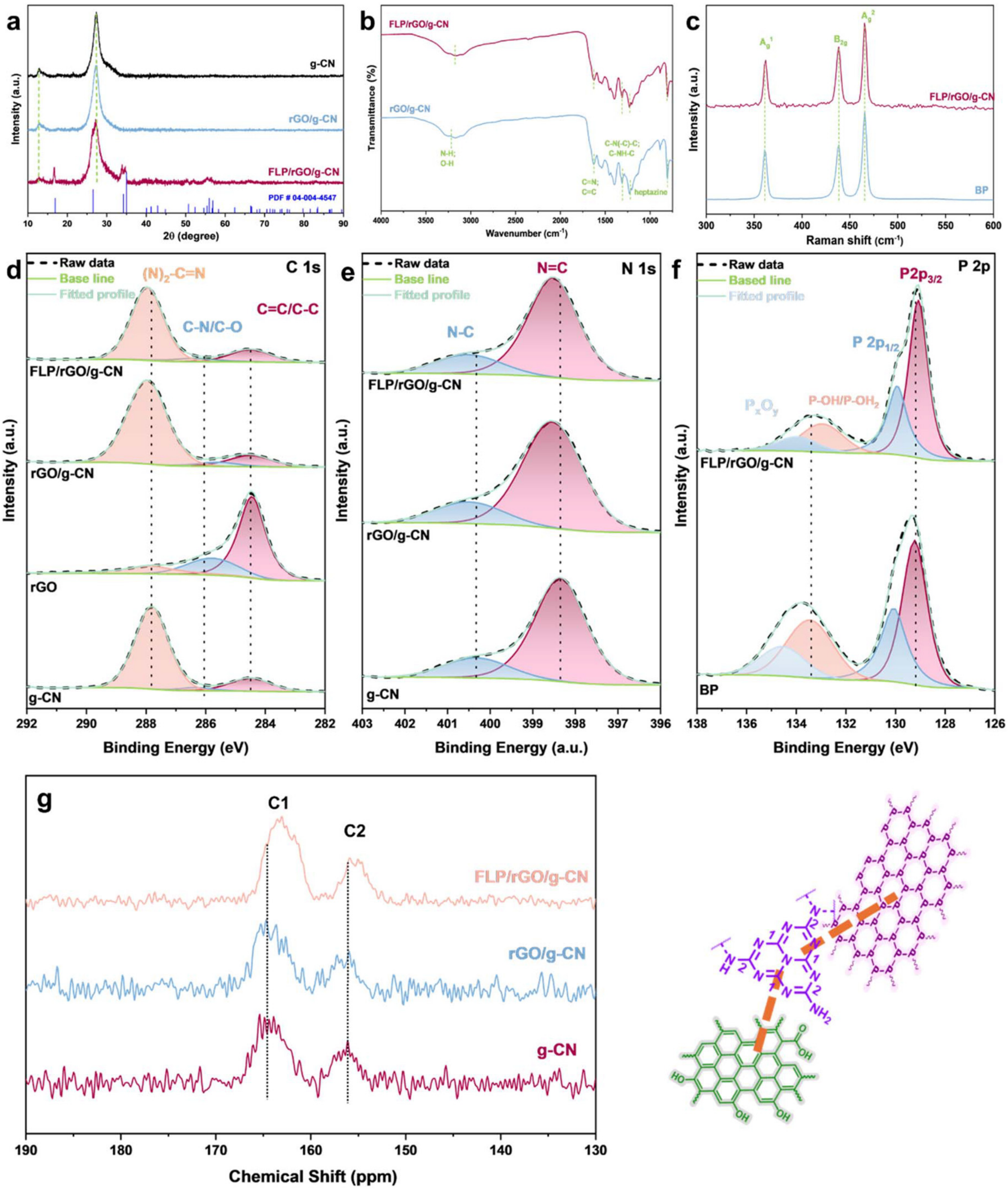

Fig. 1 (a) XRD patterns of g-CN, rGO/g-CN, and FLP/rGO/g-CN, (b) FTIR spectra of rGO/g-CN and FLP/rGO/g-CN, (c) Raman spectra of BP and FLP/rGO/g-CN, high-resolution (d) C 1s XPS spectra of g-CN, rGO, rGO/g-CN and FLP/rGO/g-CN, high-resolution (e) N 1s XPS spectra of g-CN, rGO/g-CN and FLP/rGO/g-CN and high-resolution (f) P 2p XPS spectra of FLP and FLP/rGO/g-CN, and (g) ^{13}C CP MAS NMR of g-CN, rGO/g-CN and FLP/rGO/g-CN.

spectra are presented in Fig. 1c. Given the low concentration of rGO and the Raman-inactive nature of g-CN, only the characteristic peaks associated with FLP were observed. Specifically, the peaks corresponding to the A_g^1 (out-of-plane), B_{2g} (in-plane), and A_g^2 (in-plane) phonon modes of FLP were clearly identified.[37] Notably, the A_g^1 phonon mode exhibited a 1.5 cm^{-1} red shift in the ternary FLP/rGO/g-CN heterojunction compared to pristine FLP, which is attributed to interlayer distance modifications resulting from interactions within the heterostructure. This shift provides additional evidence for the successful formation of the designed ternary heterojunction.

X-ray photoelectron spectroscopy (XPS) analysis was conducted to investigate the surface chemical composition and environment of the synthesized FLP/rGO/g-CN heterojunction and its pristine materials. The survey XPS spectrum (Fig. S1) confirmed the presence of P 2p and P 2s peaks characteristic of FLP, C 1s and O 1s peaks associated with rGO and g-CN and the N 1s peak originating from g-CN. In both the high-resolution C 1s spectra of rGO/g-CN and FLP/rGO/g-CN, the peak at 284.5 eV attributed to C–C/C=C increased in intensity upon incorporation of rGO, and all carbon-related peaks shifted to higher binding energy compared to pristine g-CN.[42,43] The high-resolution C 1s spectrum (Fig. 1d) also displayed two additional peaks corresponding to C–N (285.9 eV), and (N)$_2$–C=N (288.0 eV), confirming the presence of sp^2-hybridized carbon and carbon–nitrogen bonds in the ternary heterojunction. In the high-resolution N 1s spectrum (Fig. 1e), the peaks at 398.6 and 400.4 eV were attributed to N=C and N–C bonds, respectively, which are characteristic of the heptazine units in g-CN.[44] The high-resolution P 2p spectrum (Fig. 1f) exhibited peaks at 129.0 and 129.9 eV, corresponding to P $2p_{3/2}$ and P $2p_{1/2}$ of FLP, respectively.[45] Additionally, peaks at 133.2 and 134.1 eV were assigned to P–OH and P$_x$O$_y$ species, indicating interactions between phosphorus in FLP and other components of the heterojunction.[46] Notably, compared to pristine FLP, all P 2p peaks shifted to lower binding energy, while C 1s and N 1s peaks shifted to higher energy. These opposite shifts indicate electron transfer from rGO/g-CN to FLP, providing strong evidence of interfacial electronic coupling and a well-established heterojunction. ^{13}C cross-polarization magic-angle-spinning solid-state NMR (^{13}C CP MAS ssNMR) spectroscopy was performed to further investigate how rGO and BP influence the structure of g-CN and their positioning within the composite (Fig. 1g). Pristine g-CN exhibits two main characteristic resonances at 156.1 ppm (CN$_2$-(NH$_x$), labeled C-2) and 163.9 ppm (CN$_3$, labeled C-1).[47] Upon incorporation of rGO, the C-1 signal shifts to higher frequency (164.7 ppm), while C-2 remains essentially unchanged at 155.9 ppm. This downfield shift of C-1 is consistent with the presence of polar, electron-deficient functional groups at the edges of the rGO layers. In contrast, introduction of FLP into the binary rGO/g-CN heterojunction causes C-1 to shift to a lower frequency (163.1 ppm), even below that of pristine g-CN, whereas the C-2 resonance remains unaltered at 155.9 ppm. Owing to these chemical environment changes observed for the C-1 peak, both rGO and FLP are inferred to be positioned at or interacting with the central triazine rings of g-CN.[36] These spectral changes clearly indicate strong interfacial coupling among the components and support the occurrence of electron transfer from FLP to the rGO/g-CN system, in agreement with the XPS analysis.

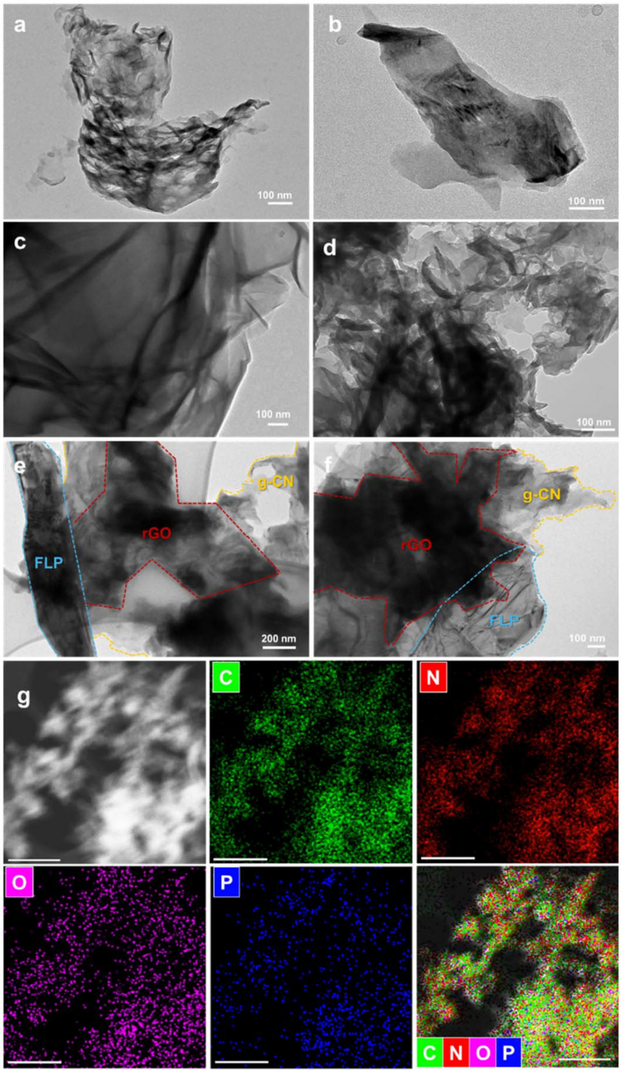

Fig. 2 TEM images of (a) g-CN, (b) FLP, (c) rGO, (d) rGO/g-CN, (e) and (f) FLP/rGO/g-CN; (g) HAADF-STEM image and associated elemental mappings (the scale bars are all 500 nm).

Transmission electron microscopy (TEM) analysis was performed to examine the morphological features of g-CN, FLP, rGO, the binary rGO/g-CN heterojunction and the ternary FLP/rGO/g-CN heterojunction, with representative TEM images at different magnifications presented in Fig. 2. The mesoporous nanostructure of g-CN is clearly observed in Fig. 2a, whereas the smooth surface and layered morphology of FLP are evident in Fig. 2b. While the sheet-like morphology of rGO is evident in Fig. 2c, the image in Fig. 2d confirms the successful incorporation of rGO, displaying its thin, layered structure intimately attached to the mesoporous framework of g-CN. Furthermore, in Fig. 2e and f, morphological features of the ternary FLP/rGO/g-CN heterostructure were identified: blue dashed lines highlight the distinctive traces of FLP, the dark regions outlined by red dashed lines correspond to rGO, and the yellow circular dashed lines indicate the g-CN nanolayers. High-Angle Annular Dark Field Scanning Transmission Electron Microscopy (HAADF-STEM) analysis, along with correlative Energy Dispersive Spectroscopy (EDS) elemental mapping, was performed to investigate the elemental distribution and confirm the formation of heterojunctions. The HAADF-STEM and EDS mapping results for the rGO/g-CN heterojunction are presented in Fig. S2, while those for the FLP/rGO/g-CN heterojunction are shown in Fig. 2g. As depicted in Fig. S2, the uniform distribution of C, N, and O elements throughout the structure provides strong evidence of the successful synthesis of the binary rGO/g-CN heterojunction. Furthermore, in Fig. 2g, the homogeneous spatial distribution of C, P, and N elements in the HAADF-STEM image and the corresponding EDS elemental maps confirms the successful fabrication of the ternary FLP/rGO/g-CN heterojunction. The uniform integration of these elements suggests well-established interfacial interactions among the components, which are critical for efficient charge transfer and enhanced photocatalytic performance.

To evaluate the enhancement in photophysical properties achieved through heterojunction formation, UV-vis DRS, photoluminescence (PL), and time-resolved PL (TRPL) analyses were conducted for single (g-CN), binary (rGO/g-CN), and ternary (FLP/rGO/g-CN) heterojunctions. As illustrated in Fig. 3a, the incorporation of rGO led to increased light absorption, particularly beyond 450 nm, compared to pristine g-CN. Furthermore, the addition of FLP, which interacts with light across a broader range from the visible to NIR region, significantly enhanced light absorption, resulting in a heterojunction with superior optical absorption properties. The Tauc plots (Fig. 3b) revealed a reduction in the band gap of g-CN from 2.77 to 2.66 eV in the FLP/rGO/g-CN heterojunction, indicating lower energy requirements for charge excitation. This enhanced charge separation was further confirmed using PL spectra (Fig. 3c), where a substantial decrease in PL emission intensity from g-CN to FLP/rGO/g-CN suggested effective suppression of photogenerated electron–hole recombination. Additionally, TRPL measurements (Fig. 3d) demonstrated a decrease in the average electron lifetime (τ) from 6.67 ns (g-CN) to 6.21 ns (rGO/g-CN), highlighting the role of rGO as a conductive pathway for accelerated charge transfer. Upon the incorporation of FLP, the electron lifetime increased to 6.51 ns, implying that while rGO facilitated rapid charge transport, the FLP component contributed to improved charge separation and suppressed charge recombination. These findings suggest that the FLP/rGO/g-CN ternary heterojunction exhibits enhanced light absorption, efficient charge separation, and minimized photogenerated electron–hole recombination, making it a highly efficient catalyst for C–H activation reactions under light irradiation.

Photocatalytic performance

To investigate the photocatalytic activity of FLP/rGO/g-CN ternary heterojunctions in the photoredox C–H arylation, the reaction between furan (**1a**) and 4-chlorophenyl diazonium salt **2a** was selected as the model reaction. Initially, FLP, rGO and g-CN were tested separately to understand the activity of pristine materials, yielding the desired product **3a** with yields of 42%, 27% and 53%, respectively (Table 1, entries 1–3). Subsequently, the binary combination of rGO and g-CN was

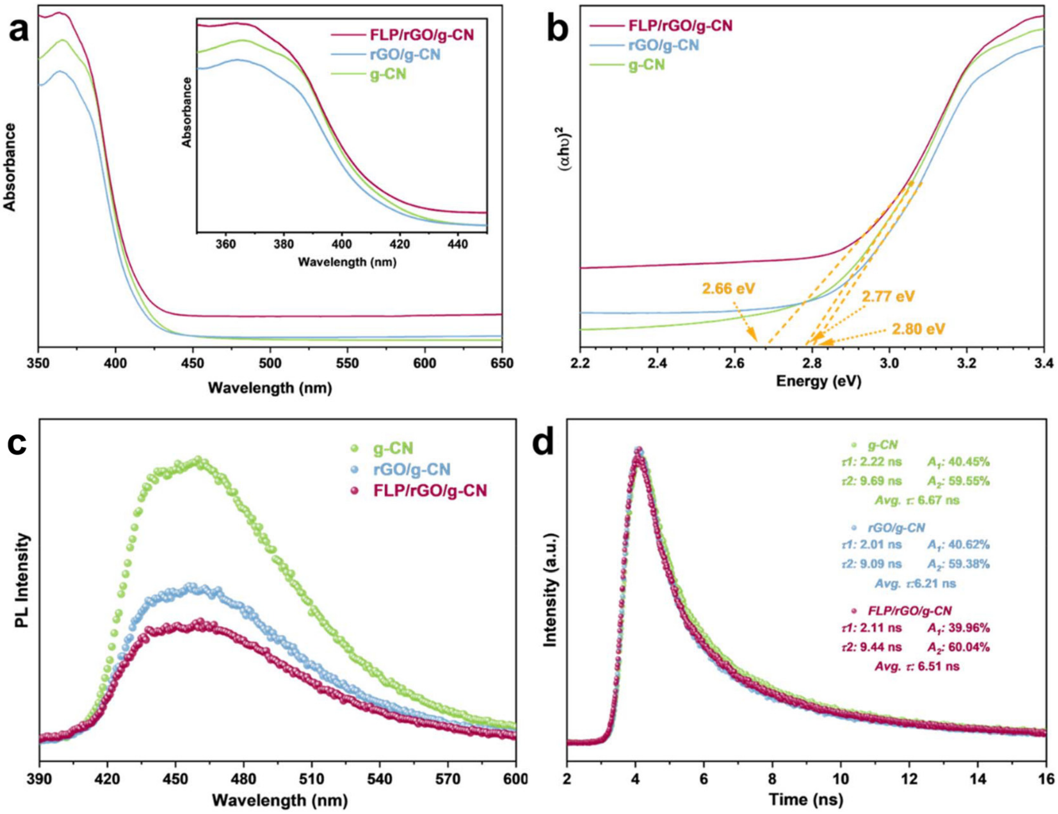

Fig. 3 (a) UV-visible absorbance spectra, (b) Tauc plot, (c) PL spectra, and (d) TRPL spectra of g-CN, rGO/g-CN, and FLP/rGO/g-CN.

Table 1 Optimization of reaction conditions using FLP/rGO/g-CN and the pristine materials[a]

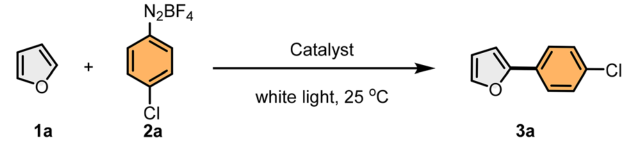

Entry	**1a** (equiv.)	Catalyst	Solvent	Time (min)	Yield[e] (%)
1	20	FLP	DMSO	120	42[b]
2	20	rGO	DMSO	120	27[b]
3	20	g-CN	DMSO	120	53[b]
4	20	rGO/g-CN	DMSO	120	89[b]
5	20	rGO/g-CN	DMSO	60	89[b]
6	20	rGO/g-CN	DMSO	90	88
7	20	FLP/rGO/g-CN (5%)	DMSO	90	85
8	20	FLP/rGO/g-CN (30%)	DMSO	90	90
9	10	FLP/rGO/g-CN (30%)	DMSO	90	40
10	20	FLP/rGO/g-CN (30%)	DMSO	90	89[b]
11	30	FLP/rGO/g-CN (30%)	DMSO	90	90
12	40	FLP/rGO/g-CN (30%)	DMSO	60	91
13	**40**	**FLP/rGO/g-CN (30%)**	**DMSO**	**90**	**94**
14	40	FLP/rGO/g-CN (40%)	DMSO	90	88
15	40	—	DMSO	90	Trace
16	40	FLP/rGO/g-CN (30%)	THF	90	27
17	40	FLP/rGO/g-CN (30%)	DMF	90	54
18	40	FLP/rGO/g-CN (30%)	CH_3CN	90	47
19	40	FLP/rGO/g-CN (30%)	DMSO	90	85[c]
20	40	FLP/rGO/g-CN (30%)	DMSO	90	90[d]
21	40	FLP/rGO/g-CN (30%)	DMSO	90	—[f]

[a] The reaction was carried out with **1a** (in varying equiv.), **2a** (0.25 mmol), and catalyst (5 mg) in a solvent (1.0 mL) under white light (150 W) irradiation at 25 °C. [b] Catalyst (10 mg). [c] Solvent 0.5 mL. [d] Solvent 2.0 mL. [e] Yields were determined by ^1H NMR analysis using 1,3-dinitrobenzene as the internal standard. [f] Dark conditions.

evaluated in the model reaction by varying the reaction time and photocatalyst amount. The product **3a** was obtained in 89% yield using 10 mg of photocatalyst in 2 h (Table 1, entry 4). Remarkably, reducing the reaction time to 1 h did not affect the efficiency (Table 1, entry 5). Once the photocatalyst amount was reduced to 5 mg of rGO/g-CN, the product yield remain intact (Table 1, entry 6). Following the results of the binary heterojunctions, the effectiveness of the ternary heterojunction photocatalysts with varying FLP contents was evaluated in the model C–H arylation reaction. In the reaction performed with FLP/rGO/g-CN (5 wt% FLP) ternary heterojunctions, the product **3a** was obtained with an 85% yield (Table 1, entry 7). When the FLP content was increased (30 wt%), a yield increase of up to 90% was observed (Table 1, entry 8). Investigation of the heteroarene loading revealed reducing the amount of furan to 10 equivalents led to a dramatic decrease in yield to 40% (Table 1, entry 9). It was determined that further doubling the photocatalyst amount from 5 mg to 10 mg did not significantly affect the yield (Table 1, entry 10). Furthermore, increasing the heteroarene loading from 20 to 30 equivalents afforded comparable yields (Table 1, entry 11). Notably, using 40 equivalents of **1a** resulted in 91% yield within 1 h and 94% yield in 90 min (Table 1, entries 12 and 13). When the FLP amount in the FLP/rGO/g-CN ternary photocatalyst was increased from 30% to 40%, the product was obtained in 88% yield (Table 1, entry 14). In the absence of the photocatalyst, a trace amount of the product was observed (Table 1, entry 15). To gain further insight into the catalyst effect, the reaction was evaluated in various solvents and **3a** was obtained in 27% yield in THF, 54% yield in DMF, and 47% yield in CH_3CN (Table 1, entries 16–18). It was clearly observed that the reaction gave the best result with DMSO (Table 1, entry 13). Consequently, the optimized reaction conditions were established as 25 °C for 90 min using 40 equivalents of furan (**1a**) and 0.25 mmol aryl diazonium **2a**. Regarding the effect of reaction concentration on the product yield, the reaction yield was 85% in 0.5 mL of DMSO, while the yield was determined to be 90% when the reaction mixture was diluted to 2.0 mL (Table 1, entries 19 and 20). When the reaction was carried out in the dark, no product formation was observed (Table 1, entry 21). Another reason for choosing DMSO as the reaction solvent is our previous experience and examples in the literature.[16,48,49] In related direct C–H photoarylation reactions with aryl diazonium salts, DMSO produced positive outcomes compared to other solvents likely due to its ability to solubilize aryl diazonium salts and heteroarenes and to facilitate the formation of photoactive intermediates under visible-light irradiation. In addition, this solvent provides an efficient environment for the exfoliation of the ternary heterojunction.

With the optimum reaction conditions in hand, the substrate scope of the FLP/rGO/g-CN ternary heterojunction was investigated. As illustrated in Table 2, various aryl diazonium salts bearing a wide range of electron-withdrawing and electron-donating groups were studied using heteroarenes (furan and thiophene). Arylation products **3b** and **3c**, with aryl diazonium salts containing *para*- and *meta*-nitro, were obtained in 76% and 73% yields, respectively. In the case of $-CF_3$ (*para*-, *meta*-) substituted aryl diazonium salts, the C–H arylation products were formed with very good yields (**3d** and **3e**, 80% and 82%, respectively). The reactions of aryldiazonium salts substituted with electron-donating groups –Me and –OMe (*para*-, *meta*-) with furan delivered the arylation products in modest to very good yields (**3f**–**3i**, 38%–87%, respectively). Here, it was observed that the photocatalyst is more effective with aryl diazonium salts bearing *para*-substituted electron-donating groups (–Me, –OMe) compared to aryl diazonium salts bearing the *meta*-substituted counterparts. Halogen-containing aryl diazonium salts reacted smoothly, and the corresponding products were obtained in excellent yields (**3j** and **3k**, 96% and 92%, respectively). The reaction of phenyl diazonium salt and furan yielded **3l** in 71% yield. Based on the obtained results, it was observed that the reaction proceeded in better yields in the presence of aryl diazonium salts containing an electron-withdrawing group.

The reactions of thiophene and aryl diazonium salts were conducted for 4 hours to obtain better yields. The reaction of thiophene and aryl diazonium salt containing 4-Cl yielded the arylation product **4a** in 77% yield. Aryl diazonium salts

Table 2 The substrate scope of heteroarenes and aryl diazonium salts[a,b]

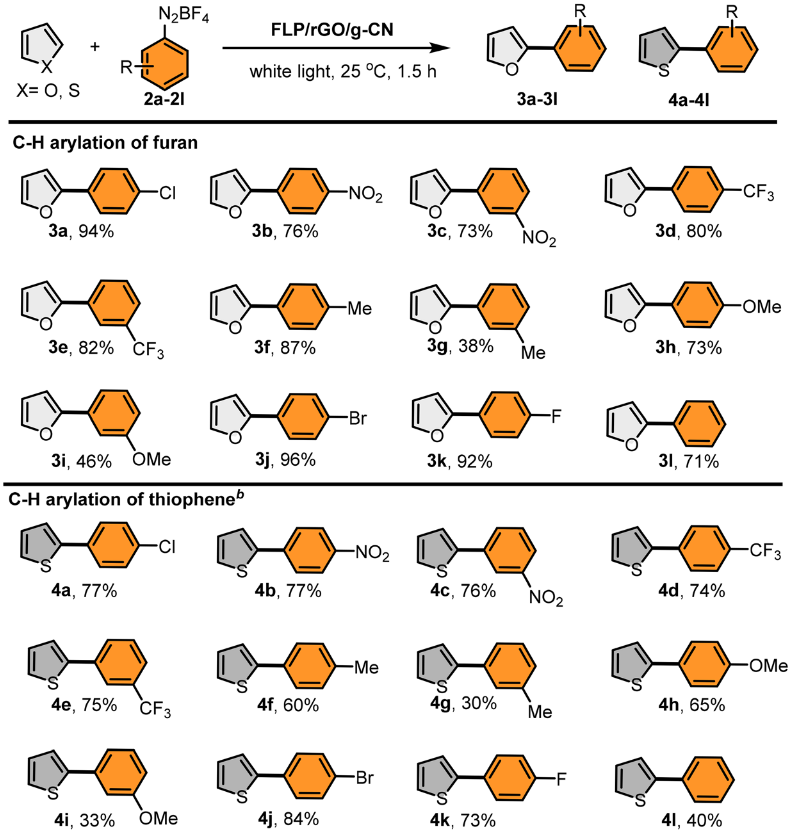

[a] The reactions were carried out with heteroarenes (40 equiv.), aryl diazonium salts (0.25 mmol), and FLP/rGO/g-CN (5 mg) in DMSO (1.0 mL) under white light (150 W) irradiation at 25 °C for 1.5 h. [b] The reaction was conducted for 4 h.

bearing nitro (*para*-, *meta*-) were converted to the corresponding arylation products (**4b** and **4c**) in 77% and 76% yields, respectively. Similarly, C–H arylation products **4d** and **4e** were obtained from $-CF_3$ (*para*-, *meta*-) substituted aryl diazonium salts in 74% and 75% yields, respectively. The desired products (**4f**–**4i**) were obtained in 30–65% yields from the reaction between thiophene and aryl diazonium salts containing –Me and –OMe groups (*para*-, *meta*-). Additionally, the corresponding arylation products from aryl diazonium salts bearing halogens resulted in good yields (**4j** and **4k**, 84% and 73% yields, respectively). Conversely, the yield dropped to 40% for the unsubstituted phenyl derivative **4l**, which is significantly lower than the yield obtained for its furan-based counterpart.

To investigate the effect of photocatalyst regioselectivity on C–H arylation with aryl diazonium salts, various substituted heteroarenes were tested (Table 3). With the optimal conditions in hand, the target products **6aa** and **6ab** were obtained from the reaction of methyl and ethyl substituted furan and 4-chloro aryl diazonium salt in 42% and 33% yields, respectively. Furan-2-carboxaldehyde and 4-nitro substituted aryl diazonium salt provided the arylation product **6ac** in 29% yield. It was observed that methyl- and ethyl-substituted thiophene derivatives provided lower results for the related arylation products. Arylation products **6ba** and **6bb** were obtained with lower yields (8% and 17%, respectively). Finally, the arylation product **6bc** was observed in trace amounts in the reaction with thiophene-2-carboxaldehyde and 4-chloro aryl diazonium salt. Steric and mechanistic effects are likely the cause of the low yields for C2-substituted heteroarenes (Table 3). Alkyl substitution at the C2 position of the heteroarene resulted in the obtaining of the corresponding arylation products with lower yields. Additionally, thiophene derivatives display lower reactivity toward radical addition compared to furan rings because of their higher aromatic stabilization, resulting in lower yields for thiophenes.[16,50]

To increase the diversity, various (hetero)arenes were tested to investigate the effect of the regioselective photocatalysis on C–H arylation with aryl diazonium salts (Table 4). Under optimum conditions, the reaction of *N*-Boc pyrrole and halogen-containing aryl diazonium salts yielded the Cl-substituted product **8aa** in 35% yield, while the Br-substituted arylation product **8ab** in 49% yield. When the reaction time was extended to 5 h, the arylation product **8aa** was obtained in 42% yield. Arylation products **8ac** and **8ad**, with aryl diazoniums containing *para*- and *meta*-nitro, were obtained in 35% and 48% yields, respectively. When the photocatalytic performance was evaluated using benzene as an arene, it revealed an improvement in the yields. The 4-Cl-substituted product **8ba**

Table 3 The substrate scope of various heteroarenes and aryl diazonium salts[a]

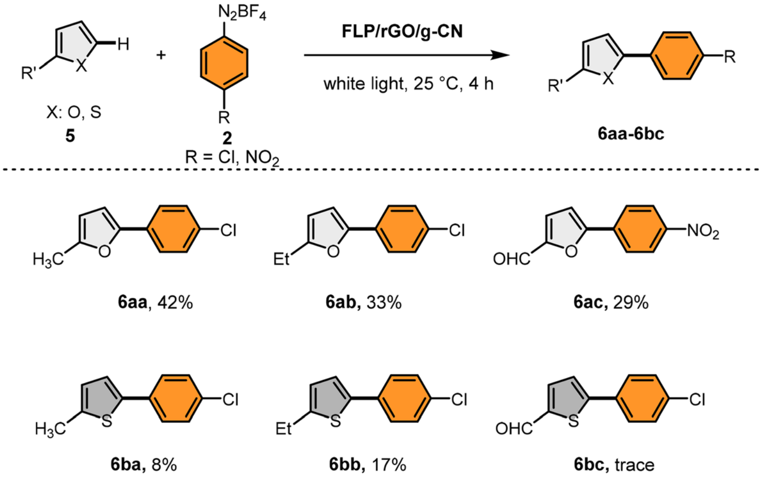

[a] The reactions were carried out with heteroarenes (5.0 equiv.), aryl diazonium salts (0.25 mmol), and FLP/rGO/g-CN (5 mg) in DMSO (1.0 mL) under white light (150 W) irradiation at 25 °C for 4 h. Yields were detected by ^{1}H NMR analysis using 1,3-dinitrobenzene as the internal standard.

Table 4 The substrate scope of *N*-Boc pyrrole and benzene with aryl diazonium salts[a,b]

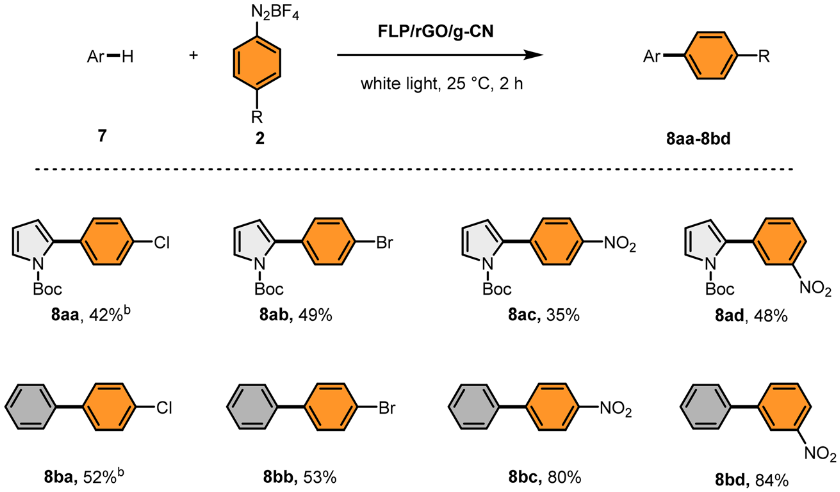

[a] The reactions were carried out with *N*-Boc pyrrole (1.0 equiv.) or benzene (40 equiv.), aryl diazonium salts (0.25 mmol), and FLP/rGO/g-CN (5 mg) in DMSO (1.0 mL) under white light (150 W) irradiation at 25 °C for 2 h. [b] Reaction was conducted for 5 h. Yields were detected by ^{1}H NMR analysis using 1,3-dinitrobenzene as the internal standard.

was obtained in 40% yield, while the 4-Br-substituted arylation product **8bb** was obtained in 53% yield. A longer reaction time (5 h) afforded **8ba** in 52% yield. From the reaction of nitro (*para*-, *meta*-) substituted aryl diazonium salts, arylation products **8bc** and **8bd** were obtained in good yields (80% and 84% yields, respectively). Interestingly, although the arylation products were obtained from aryl diazonium salts bearing 4-Cl and 4-Br are competitive, benzene arylation products in the presence of aryl diazonium salts containing the nitro group were observed in higher yields compared to *N*-Boc-protected pyrrole.

Photocatalytic mechanism

Understanding the electronic band structures of the individual semiconductors, as well as the nature of the heterojunction formed between them, is essential for elucidating the radical-driven photochemical mechanism. The band edge positions were determined from XPS-valence band (VB) and Mott–Schottky (MS) analyses, where the VB levels of g-CN and FLP were obtained as +2.02 V and +0.32 V *vs.* NHE, and the corresponding conduction band (CB) levels were derived as −0.65 V and −0.60 V *vs.* NHE, respectively, as shown in Fig. 4a–c and SI

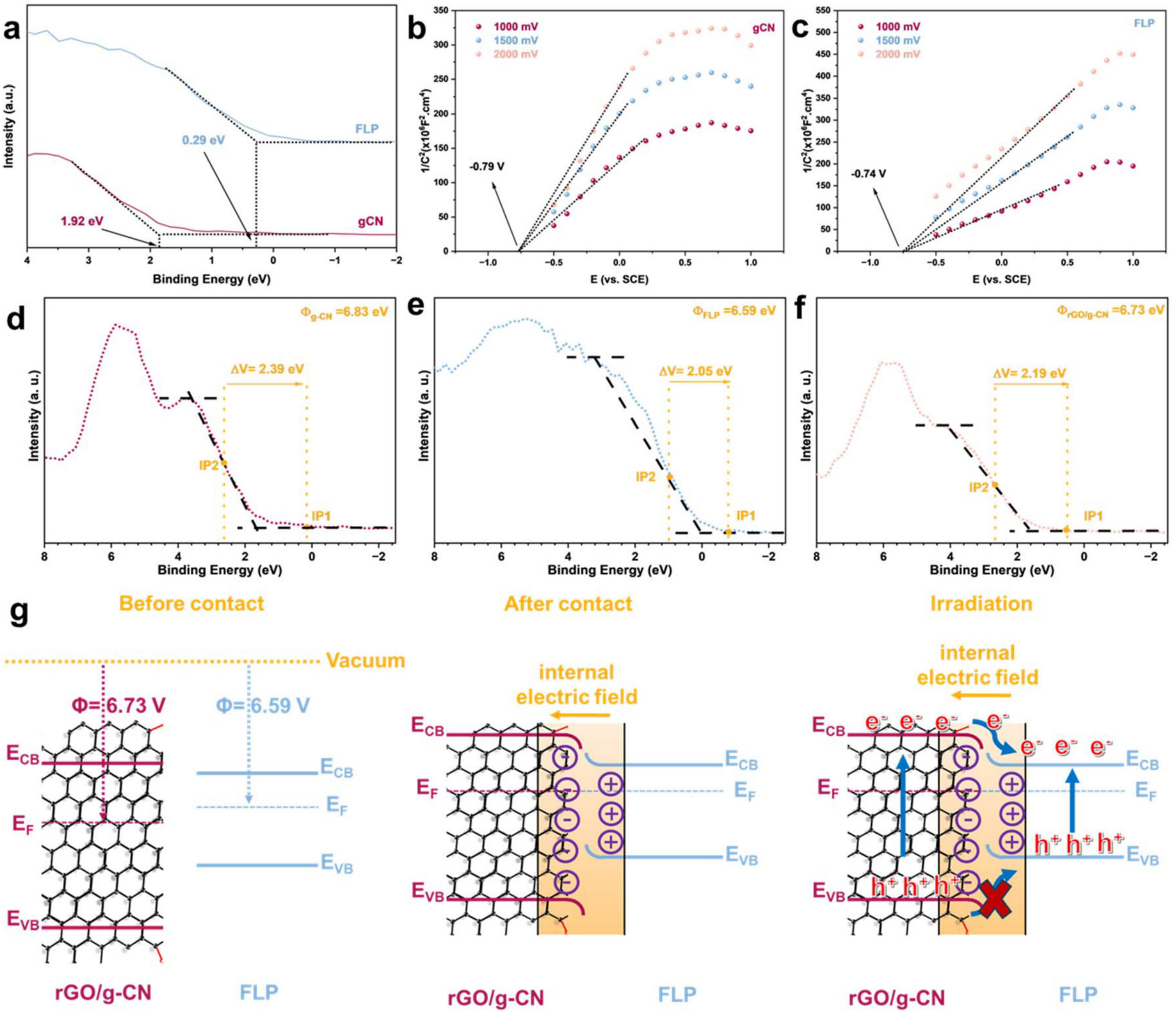

Fig. 4 (a) XPS-VB analyses of g-CN and FLP; MS analyses of (b) g-CN and (c) FLP; work functions of (d) g-CN, (e) FLP, and (f) rGO/g-CN, (g) IEF between semiconductors before and after contact, and under irradiation, resulting in the bending of band edges for rGO/g-CN and FLP.

Note 1. Overall, the resulting band alignment and energy landscape are illustrated in the comprehensive band diagram presented in Fig. S3.

In addition to band-edge analysis, work function measurements were used to clarify the interfacial charge-transfer direction within the heterostructure. XPS-VB-derived work functions[51] for g-CN, rGO/g-CN, and FLP were determined as 6.83, 6.73, and 6.59 eV, respectively (Fig. 4d–f, Fig. S4 and SI Note 2). The reduction in work function upon rGO incorporation indicates electron donation from rGO to g-CN, shifting its Fermi level (E_F) closer to the vacuum level. After incorporating FLP into the rGO/g-CN binary heterojunction, negative charges migrate from FLP (lower E_F) to rGO/gCN (higher E_F) until Fermi level equilibrium is reached, generating an intrinsic electric field at the interface. This induces downward band bending in rGO/g-CN and upward bending in FLP. Under visible-light irradiation, electrons transfer from the CB of rGO/g-CN to the CB of FLP, while holes remain in the VB of rGO/g-CN due to unfavorable band alignment (Fig. 4g). This spatial charge separation enhances carrier transport and supports a nonclassical type-I heterojunction mechanism dominated by photocatalytic reactions.

To verify the proposed single-electron transfer (SET) mechanism for the FLP/rGO/g-CN heterojunction catalyzed direct C–H arylation reaction and to elucidate the roles of photogenerated charge carriers in the reaction pathway, a series of scavenger experiments were conducted using the model reaction shown in Fig. 5a and Fig. S5a. Specifically, 1,4-benzoquinone (BQ), 2,2,6,6-tetramethylpiperidinoxyl (TEMPO), and triethanolamine (TEOA) were employed as scavengers for photogenerated electrons, radicals, and holes, respectively. In the presence of BQ, the product yield decreased significantly to 14%, highlighting the critical role of the photo-generated electrons in the photocatalytic process. When TEMPO was introduced to quench the photo-generated radical species, the yield similarly dropped to 17%, indicating that the reaction proceeds *via* a radical-mediated pathway. To support the involvement of a radical pathway in this transformation, the corres-

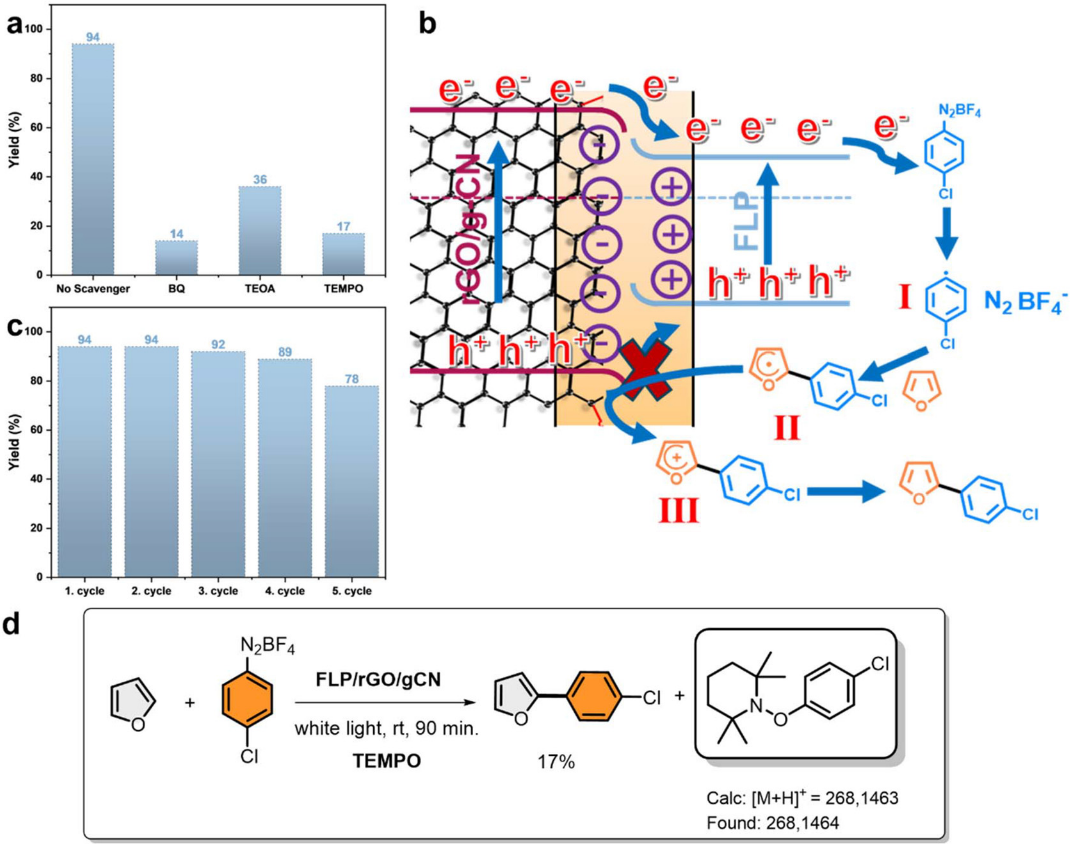

Fig. 5 (a) Scavenger test with the FLP/rGO/g-CN heterojunction. (b) Plausible mechanism of the C–H arylation reaction using FLP/rGO/g-CN. (c) The reusability experiments of FLP/rGO/g-CN in the C–H arylation reaction. (d) Radical quenching experiment with TEMPO.

ponding radical scavenger agent was detected by high-resolution mass spectrometry (HRMS) with the addition of TEMPO (Fig. 5d and S5b). HMRS data clearly showed the formation of TEMPO-aryl radical coupling product. In contrast, the addition of TEOA, a known hole scavenger, led to a comparatively modest decrease in product yield to 36%, suggesting that photogenerated holes play a less significant role in the overall reaction. This result is related to the oxidation potential of TEOA, which is approximately 0.82 V *vs*. NHE[31] and only the VB of g-CN can accept an electron from TEOA, whereas the FLP cannot. Instead, the enhanced photocatalytic performance, along with the exceptional optical and morphological characteristics of the synthesized ternary heterojunction, can be attributed to the formation of a nonclassical type-I heterojunction as earlier discussed and confirmed with control experiments.[31] Based on this understanding, a plausible mechanism for the direct C–H arylation reaction is proposed in Fig. 5b, which supports the involvement of a single photogenerated electron originating from the FLP/rGO/g-CN heterojunction. Upon light irradiation, photogenerated electrons from the FLP/g-CN component are transferred to rGO, which facilitates rapid electron transport due to its high conductivity. These electrons subsequently interact with the diazonium salt **2a**, initiating a SET process that generates the aryl radical species **I**. This aryl radical **I** is then captured by the heteroarene, leading to the formation of radical intermediate **II**. The intermediate is further oxidized to form the cationic species **III** *via* electron transfer to the photogenerated holes at the VB of g-CN. Finally, deprotonation of the cationic intermediate restores aromaticity, resulting in the formation of the desired arylated product **3a**.

After examining the mechanistic studies, the reusability of the FLP/rGO/g-CN ternary heterojunction was investigated in the model reaction, photoredox C–H arylation of furan (**1a**) with 4-chlorobenzene diazonium salt (**2a**), up to five runs (Fig. 5c). In the first two runs, an excellent yield of 94% was observed for the arylation product. In the third run, a slight decrease was observed to 92% and in the fourth run, to 89%. Finally, in the fifth run, the C–H arylation product resulted in a yield of 78%. As a result, the photocatalyst demonstrated its durability and enhanced chemical stability by being reusable over five consecutive cycles, which is one of the most important criteria of sustainable chemistry. After the reusability experiments, the structural and morphological integrity of the FLP/rGO/g-CN photocatalyst were assessed by performing XRD and TEM analyses (Fig. S6 and S7). As shown in the XRD pattern of the FLP/rGO/g-CN heterojunction after the fifth run (Fig. S6), no significant changes were observed in the crystalline structure of the ternary heterojunction. Furthermore, the TEM image of the ternary heterojunction (Fig. S7) revealed that the layered architecture of the FLP/rGO/g-CN composite remained intact, with no noticeable degradation or morphological distortion. This preserved layered morphology is believed to contribute significantly to the catalyst's excellent reusability and long-term stability under photocatalytic conditions.

As summarized in Table S1, the FLP/rGO/g-CN heterojunction photocatalyst demonstrated broad substrate compatibility toward the photoredox C–H arylation of heteroarenes, delivering superior catalytic performance for several derivatives and comparable efficiencies for others when benchmarked against previously reported homogeneous, heterogeneous, and metal-based photocatalytic systems. Importantly, these catalytic results were achieved using a fully metal-free and heterogeneous photocatalyst, highlighting the effectiveness of the rationally engineered ternary heterojunction for sustainable photoredox transformations.

Conclusions

In summary, we have demonstrated the high efficiency of a novel, metal-free FLP/rGO/g-CN ternary heterojunction photocatalyst for the direct C–H arylation of heteroarenes (furans and thiophenes) under visible-light irradiation. Advanced characterization techniques confirmed the formation of a strongly coupled FLP/rGO/g-CN ternary heterojunction, where synergistic interactions between the components promote efficient separation and migration of photogenerated charges, ultimately leading to markedly improved photocatalytic performance. Systematic optimization revealed that the catalyst containing 30 wt% FLP exhibited the highest activity, outperforming both individual constituents and binary systems. Satisfyingly, the presence of both electron-withdrawing and electron-donating groups in aryl diazonium salts, particularly halogen-bearing substituents, afforded the corresponding arylation products in excellent yields (up to 96%) for arylation products of furan derivatives. While the thiophene derivatives yielded slightly lower conversions, electron-withdrawing and halogen groups still allowed successful transformation with yields reaching up to 84%. ssNMR analysis demonstrates pronounced interactions between the central nitrogen atoms of the tri-s-triazine units and the FLP species as well as rGO, accompanied by an increase in local electron density in this region. This synergistic coupling at the active sites underpins the enhanced photocatalytic activity compared to the pristine materials, stemming from favorable alterations in both the structural architecture and electronic characteristics. We performed a series of scavenger experiments to elucidate the role of the FLP/rGO/g-CN heterojunction in C–H functionalization mechanism. These results revealed that the ternary system operates through an efficient nonclassical type-I heterojunction and the heterogeneous nature of the FLP/rGO/g-CN catalyst was further validated through recycling tests, which showed remarkable stability with no significant activity loss over five consecutive reaction cycles. We believe that this study will open a new direction for extending the use of the FLP/rGO/g-CN heterojunction system along with many other possible metal-free ternary heterojunctions to other photoredox transformations.

Conflicts of interest

There are no conflicts to declare.

Data availability

The data supporting this article have been included as part of the supplementary information (SI). Supplementary information: materials, methods, additional characterization of catalysts (XPS, HAADF-STEM image, band potentials, XPS-VB, postcharacterization), the products (^{1}H NMR and ^{13}C NMR spectra of the yielded compounds), mass spectra and comparison table. See DOI: **https://doi.org/10.1039/d6qi00520a**.

Acknowledgements

This study was funded by the Turkish Scientific and Technical Research Council-TÜBİTAK (Project Number: 120Z622).

References

1 B. König, Photocatalysis in Organic Synthesis – Past, Present, and Future, *Eur. J. Org. Chem.*, 2017, **2017**, 1979–1981.

2 C. K. Prier, D. A. Rankic and D. W. C. MacMillan, *Visible light photoredox catalysis with transition metal complexes: Applications in organic synthesis*, American Chemical Society, 2013. DOI: **10.1021/cr300503r**.

3 X. Wang, C. Zhou, R. Shi, Q. Liu, G. I. N. Waterhouse, L. Wu, C. H. Tung and T. Zhang, Supramolecular precursor strategy for the synthesis of holey graphitic carbon nitride nanotubes with enhanced photocatalytic hydrogen evolution performance, *Nano Res.*, 2019, **12**, 2385–2389.

4 K. Zeitler, Photoredox catalysis with visible light, *Angew. Chem., Int. Ed.*, 2009, **48**, 9785–9789.

5 J. Xie, H. Jin, P. Xu and C. Zhu, When C–H bond functionalization meets visible-light photoredox catalysis, *Tetrahedron Lett.*, 2014, **55**, 36–48.

6 J. Xuan and W. J. Xiao, Visible-Light Photoredox Catalysis, *Angew. Chem., Int. Ed.*, 2012, **51**, 6828–6838.

7 M. R. Biscoe, J. Cornella, D. Kalyani and S. Neufeldt, From Established to Emerging: Evolution of Cross-Coupling Reactions, *J. Org. Chem.*, 2024, **89**, 16065–16069.

8 M. Osawa, H. Nagai and M. Akita, Photo-activation of Pd-catalyzed Sonogashira coupling using a Ru/bipyridine

complex as energy transfer agent, *Dalton Trans.*, 2007, 827–829.

9 J. Li, D. Zhang and Z. Hu, Ligand-Enabled "Two-in-One" Metallaphotocatalytic Cross Couplings, *ACS Catal.*, 2025, 1635–1654.

10 A. Janaagal, N. Sanyam, A. Mondal and I. Gupta, Robust Zinc(II)porphyrin Catalyst for Visible Light Induced C-H Arylation of Heteroarenes, *J. Org. Chem.*, 2023, **88**, 9424–9431.

11 D. Kalyani, K. B. McMurtrey, S. R. Neufeldt and M. S. Sanford, Room-temperature C-H arylation: Merger of Pd-catalyzed C-H functionalization and visible-light photocatalysis, *J. Am. Chem. Soc.*, 2011, **133**, 18566–18569.

12 X. Zhang, Y. Mei, Y. Li, J. Hu, D. Huang and Y. Bi, Visible-Light-Mediated Functionalization of Aryl Diazonium Salts, *Asian J. Org. Chem.*, 2021, **10**, 453–463.

13 P. Schroll, D. P. Hari and B. König, Photocatalytic Arylation of Alkenes, Alkynes and Enones with Diazonium Salts, *ChemistryOpen*, 2012, **1**, 130–133.

14 L. Gu, C. Jin and J. Liu, Metal-free, visible-light-mediated transformation of aryl diazonium salts and (hetero)arenes: An efficient route to aryl ketones, *Green Chem.*, 2015, **17**, 3733–3736.

15 L. He, G. Qiu, Y. Gao and J. Wu, Removal of amino groups from anilines through diazonium salt-based reactions, *Org. Biomol. Chem.*, 2014, **12**, 6965–6971.

16 D. P. Hari, P. Schroll and B. König, Metal-free, visible-light-mediated direct C-H arylation of heteroarenes with aryl diazonium salts, *J. Am. Chem. Soc.*, 2012, **134**, 2958–2961.

17 J. D. Lasso, D. J. Castillo-Pazos and C. J. Li, Green chemistry meets medicinal chemistry: a perspective on modern metal-free late-stage functionalization reactions, *Chem. Soc. Rev.*, 2021, **50**, 10955–10982.

18 X. Cai, H. Liu, L. Zhi, H. Wen, A. Yu, L. Li, F. Chen and B. Wang, A g-C3N4/rGO nanocomposite as a highly efficient metal-free photocatalyst for direct C–H arylation under visible light irradiation, *RSC Adv.*, 2017, **7**, 46132–46138.

19 H. Y. Song, J. Jiang, C. Wu, J. C. Hou, Y. H. Lu, K. L. Wang, T. B. Yang and W. M. He, Semi-heterogeneous g-C3N4/NaI dual catalytic C–C bond formation under visible light, *Green Chem.*, 2023, **25**, 3292–3296.

20 K. Poonia, V. Soni, S. Sonu, P. Singh, V. Chaudhary, S. Thakur, V. H. Nguyen, Q. Van Le and P. Raizada, Metal-free defects in 2D Nanocarbons toward photocatalytic processes: Revolutionizing solar-to-energy conversion, *Appl. Energy*, 2025, **382**, 125195.

21 Y. Ying, K. Fan, Z. Lin and H. Huang, Facing the "Cutting Edge:" Edge Site Engineering on 2D Materials for Electrocatalysis and Photocatalysis, *Adv. Mater.*, 2025, **37**, 2418757.

22 R. Hu, G. C. Liao, Z. Huang, H. Qiao, H. Liu, Y. Shu, B. Wang and X. Qi, Recent advances of monoelemental 2D materials for photocatalytic applications, *J. Hazard. Mater.*, 2021, **405**, 124179.

23 B. Luo, G. Liu and L. Wang, Recent advances in 2D materials for photocatalysis, *Nanoscale*, 2016, **8**, 6904–6920.

24 Z. Lu, D. Yu, Y. Hong, G. Ma, F. Ru, T. Ge, G. Xi, L. Qin, M. Adilov, R. Ashurov, K. Ashurov and D. Chen, Recent advances and future perspectives of bismuthene: From preparation to applications, *Mater. Today*, 2024, **80**, 565–593.

25 M. Pumera and Z. Sofer, 2D Monoelemental Arsenene, Antimonene, and Bismuthene: Beyond Black Phosphorus, *Adv. Mater.*, 2017, **29**, 1605299.

26 X. Yu, W. Liang, C. Xing, K. Chen, J. Chen, W. Huang, N. Xie, M. Qiu, X. Yan, Z. Xie and H. Zhang, Emerging 2D pnictogens for catalytic applications: status and challenges, *J. Mater. Chem. A*, 2020, **8**, 12887–12927.

27 X. Ling, H. Wang, S. Huang, F. Xia and M. S. Dresselhaus, The renaissance of black phosphorus, *Proc. Natl. Acad. Sci. U. S. A.*, 2015, **112**, 4523–4530.

28 M. S. Ozer, Z. Eroglu, A. S. Yalin, M. Kılıç, U. Rothlisberger and O. Metin, Bismuthene as a versatile photocatalyst operating under variable conditions for the photoredox CH bond functionalization, *Appl. Catal., B*, 2022, **304**, 120957.

29 E. Kalay, H. Küçükkeçeci, H. Kilic and Ö. Metin, Black phosphorus as a metal-free, visible-light-active heterogeneous photoredox catalyst for the direct C-H arylation of heteroarenes, *Chem. Commun.*, 2020, **56**, 5901–5904.

30 O. Turbedaroglu, T. Kubanaliev, S. Alemdar, Z. Eroglu, H. Kilic and O. Metin, Reduced Graphene Oxide/Few-Layer Phosphorene Binary Heterojunctions as Metal-Free Photocatalysts for the Sustainable Photoredox C-H Arylation of Heteroarenes, *ACS Sustainable Chem. Eng.*, 2024, **12**, 3659–3670.

31 Z. Eroglu, M. S. Ozer, T. Kubanaliev, H. Kilic and Ö. Metin, Synergism between few-layer black phosphorus and graphitic carbon nitride enhances the photoredox C–H arylation under visible light irradiation, *Catal. Sci. Technol.*, 2022, **12**, 5379–5389.

32 A. K. Geim, Graphene: Status and Prospects, *Science*, 2009, **324**, 1530–1534.

33 Q. Xiang, J. Yu and M. Jaroniec, Graphene-based semiconductor photocatalysts, *Chem. Soc. Rev.*, 2012, **41**, 782–796.

34 A. K. Geim and K. S. Novoselov, The rise of graphene, *Nat. Mater.*, 2007, **6**, 183–191.

35 X. Wang, S. Blechert and M. Antonietti, Polymeric graphitic carbon nitride for heterogeneous photocatalysis, *ACS Catal.*, 2012, **2**, 1596–1606.

36 Z. Eroglu and O. Metin, Internal Interactions within the Complex Type-II Heterojunction of a Graphitic Carbon Nitride/Black Phosphorus Hybrid Decorated with Graphene Quantum Dots: Implications for Photooxidation Performance, *ACS Appl. Nano Mater.*, 2023, **6**, 7960–7974.

37 Z. Eroglu, B. Sündü and O. Metin, Tailoring the redox ability of carbon nitride quantum dots/reduced graphene oxide-black phosphorus (CNQDs@rGOBP) ternary heterojunctions for photodegradation of organic pollutants, *Mater. Today Sustainability*, 2023, **23**, 100418.

38 T. Kubanaliev, Z. Eroglu, M. S. Ozer and Ö. Metin, The effect of N-vacancy on the photocatalytic activity of graphitic carbon nitride in the oxidative Mannich reaction, *Catal. Sci. Technol.*, 2023, **13**, 2317–2329.

39 A. Di Liu, Z. L. Wang, L. Liu and L. Cheng, A Visible-Light-Promoted C-H Arylation and Heteroarylation of Uracil Derivatives with Diazoniums in Aqueous Conditions, *Curr. Protoc.*, 2022, **2**, 16434–16447.

40 Z. Eroglu, M. S. Ozer and O. Metin, Black Phosphorus Quantum Dots/Carbon Nitride-Reduced Graphene Oxide Ternary Heterojunction as a Multifunctional Metal-Free Photocatalyst for Photooxidation Reactions, *ACS Sustainable Chem. Eng.*, 2023, **11**, 7560–7572.

41 İ. A. Çekceoğlu, Z. Eroglu, H. Küçükkeçeci, F. Sevgi, M. Ersoz, I. H. Patir and Ö. Metin, A NIR-light-driven Black Phosphorus Based Nanocomposite for Combating Bacteria, *ChemistrySelect*, 2022, **7**, e202104137.

42 K. Ge, Y. Zhang, D. Wang, Z. Li, J. He, C. Fu, Y. Yang, M. Pan and L. Zhu, Highly Stable Reduced Graphene Oxide Wrapped Black Phosphorus Heterostructure with Superior Photocatalytic Performance under Visible Light, *ACS Appl. Mater. Interfaces*, 2020, **12**, 20035–20043.

43 K. Kumari, P. Choudhary, D. Sharma and V. Krishnan, Amine-Functionalized Graphitic Carbon Nitride as a Sustainable Metal-free Catalyst for Knoevenagel Condensation, *Ind. Eng. Chem. Res.*, 2023, **62**, 158–168.

44 Z. Eroglu, M. S. Ozer and Ö. Metin, Nitrogen-Based Imperfections in Graphitic Carbon Nitride – New Trend for Enhancing Photocatalytic Activity?, *ChemCatChem*, 2024, **16**, e202301560.

45 G. Yanalak, Z. Eroglu, S. Yılmaz, S. Z. Bas, O. Metin and I. H. Patir, Metal doped black phosphorus/molybdenum disulfide (BP/MoS2–Y (Y: Ni, Co)) heterojunctions for the photocatalytic hydrogen evolution and electrochemical nitrite sensing applications, *Int. J. Hydrogen Energy*, 2023, **48**, 14238–14254.

46 Y. Zheng, Z. Yu, H. Ou, A. M. Asiri, Y. Chen, X. Wang, Y. Zheng, Z. Yu, H. Ou, X. Wang, Y. Chen and A. M. Asiri, Black Phosphorus and Polymeric Carbon Nitride Heterostructure for Photoinduced Molecular Oxygen Activation, *Adv. Funct. Mater.*, 2018, **28**, 1705407.

47 H. Yu, R. Shi, Y. Zhao, T. Bian, Y. Zhao, C. Zhou, G. I. N. Waterhouse, L. Z. Wu, C. H. Tung and T. Zhang, Alkali-Assisted Synthesis of Nitrogen Deficient Graphitic Carbon Nitride with Tunable Band Structures for Efficient Visible-Light-Driven Hydrogen Evolution, *Adv. Mater.*, 2017, **29**, 1605148.

48 R. C. Silva, L. F. Villela, T. J. Brocksom and K. T. De Oliveira, Direct C–H photoarylation of diazines using aryldiazonium salts and visible-light, *RSC Adv.*, 2020, **10**, 31115–31122.

49 M. S. Ozer, Z. Eroglu, S. Koyuncu and O. Metin, Strategically significant synthesis of conjugated porous organic polymers via retro diazotization chemistry, *Nat. Commun.*, 2026, **17**, 3008.

50 J. Castellanos-Soriano, D. Álvarez-Gutiérrez, M. C. Jiménez and R. Pérez-Ruiz, Photoredox catalysis powered by triplet fusion upconversion: arylation of heteroarenes, *Photochem. Photobiol. Sci.*, 2022, **21**, 1175–1184.

51 J. Xiong, X. Li, J. Huang, X. Gao, Z. Chen, J. Liu, H. Li, B. Kang, W. Yao and Y. Zhu, CN/rGO@BPQDs high-low junctions with stretching spatial charge separation ability for photocatalytic degradation and H_2O_2 production, *Appl. Catal., B*, 2020, **266**, 118602.